

Cluster Formation in Contracting Molecular Clouds

E. M. Huff and Steven W. Stahler

Astronomy Department, University of California, Berkeley, CA 94720

ehuff@astro.berkeley.edu Sstahler@astro.berkeley.edu

ABSTRACT

We explore, through a simplified, semi-analytic model, the formation of dense clusters containing massive stars. The parent cloud spawning the cluster is represented as an isothermal sphere. This sphere is in near force balance between self-gravity and turbulent pressure. Self-gravity, mediated by turbulent dissipation, drives slow contraction of the cloud, eventually leading to a sharp central spike in density and the onset of dynamical instability. We suggest that, in a real cloud, this transition marks the late and rapid production of massive stars.

We also offer an empirical prescription, akin to the Schmidt law, for low-mass star formation in our contracting cloud. Applying this prescription to the Orion Nebula Cluster, we are able to reproduce the accelerating star formation previously inferred from the distribution of member stars in the HR diagram. The cloud turns about 10 percent of its mass into low-mass stars before becoming dynamically unstable. Over a cloud free-fall time, this figure drops to 1 percent, consistent with the overall star formation efficiency of molecular clouds in the Galaxy.

Subject headings: open clusters and associations: individual (Orion Nebula Cluster) — stars: formation — stars: pre-main-sequence — ISM: clouds

1. Introduction

There is growing evidence that the formation of stellar groups is a relatively slow process. More specifically, a star cluster appears within its parent molecular cloud over a period long compared to the cloud's free-fall time, as gauged by the mean gas density. Tan et al. (2006) have summarized several lines of argument leading to this conclusion. The gas clumps believed to form massive clusters look round, indicating that they are in force balance, and not a state of collapse. Massive clusters themselves have smooth density profiles, again in contrast to a dynamical formation scenario. The observed flux in protostellar outflows

indicates a slow accretion rate, and therefore a long star formation time scale. Finally, placement of young clusters in the HR diagram yields age spreads in excess of typical free-fall times (see also Palla & Stahler 2000).

Many researchers have performed direct numerical simulations of molecular clouds; their results also bear on the issue of the star formation time scale. In a typical simulation, the computational volume is filled with a magnetized, self-gravitating gas that has a turbulent velocity field. If the turbulence is only impressed initially, it dies away in a crossing time, and most of the gas condenses into unresolvably small structures (e.g., Klessen et al. 1998). Since the crossing and free-fall times are similar in a molecular cloud, some authors have concluded that all clouds produce stars rapidly, while in a state of collapse (Hartmann et al. 2001). Others have used empirical arguments to make the same point (Elmegreen 2000). This view is at odds with the observations concerning cluster-forming clouds cited above. Moreover, the simulations show that, if turbulence is driven throughout the calculation, the rate of star formation can be reduced to a more modest level (Mac Low & Klessen 2004).¹ It is plausible that the turbulence is indeed driven by the cloud’s self-gravity, a point we shall amplify later.

The emerging picture, then, is that molecular clouds both evolve and create internal clusters in a quasi-static fashion. That is, the structure as a whole is nearly in force balance, until it is eventually destroyed by the ionizing radiation and winds from the very stars it spawns. The inferred masses of all clouds larger than dense cores greatly exceed the corresponding Jeans value, evaluated using the gas kinetic temperature. Thus, self-gravity must be opposed by some force beyond the relatively weak thermal pressure gradient. The extra support is generally attributed to MHD waves generated by internal, turbulent motion (Elmegreen & Scalo 2004). This motion, which is modeled in the numerical simulations just described, imprints itself on molecular line transitions, giving them their observed, superthermal width (Arons & Max 1975; Falgarone et al. 1992).

In this paper, we follow the quasi-static contraction of a spherical, cluster-forming cloud. Contraction is facilitated by the turbulent dissipation of energy. This investigation continues and extends an earlier one that was part of our study of the Orion Nebula Cluster (ONC) (Huff & Stahler 2006, Paper I). Here we track in more detail the changing structure of a generic cloud, taken to be in near balance between self-gravity and turbulent pressure. We find that contraction eventually causes the density profile to develop a sharp, central spike.

¹The actual rate of condensation depends on the magnitude of the *sonic length*, i.e., the size scale of turbulent eddies whose velocity matches the local sound speed (Vázquez-Semadeni et al. 2003; Krumholz & McKee 2005).

Such a region of growing density is a plausible environment for the birth of massive stars (see Stahler et al. 2000).

We also track, using a simple, empirical prescription, the formation of low-mass stars in our contracting cloud. For reasonable parameter values, stellar births occur throughout the cloud over a period of order 10^7 yr. The global rate of star formation rises with time monotonically, i.e., the formation accelerates. Extended, accelerating production of stars is also found empirically when one analyzes clusters in the HR diagram (Palla & Stahler 2000). Indeed, it is not difficult to match specifically the global acceleration documented in the ONC. Here, the star formation rate depends on cloud density in the same manner as the classic Schmidt law.

In Section 2 below, we present the basic physical assumptions underlying our model. We also give a convenient, nondimensional scheme. In Section 3, we introduce our treatment of turbulent dissipation, and calculate the interior evolution of the cloud as it contracts toward the high-density state. Section 4 offers our prescription for low-mass star formation, and compares the resulting birthrate with the ONC data. Finally, Section 5 discusses the broader implications of our findings, as well as their utility for future work.

2. Formulation of the Problem

2.1. Physical Assumptions

We focus on molecular cloud clumps that are destined to produce the highest-density clusters, i.e., those containing massive stars near their centers. Shirley et al. (2003) used CS observations to study a sample of 63 clumps already containing massive stars, as evidenced by water maser emission. These clouds are nearly round, with median projected axis ratios of 1.2. It is thus a reasonable approximation, and certainly a computationally advantageous one, to take our model cloud to be spherically symmetric.

The clumps observed by Shirley et al. (2003) have a median radius of 0.32 pc and mass of $920 M_{\odot}$. A cloud of this size and mass has internal, turbulent motion well in excess of the sound speed, where the latter is based on the typical gas kinetic temperature of 10 K (Larson 1981). This bulk motion excites a spectrum of MHD waves, i.e., perturbations to the interstellar magnetic field threading the cloud (Falgarone & Puget 1986). Such waves exert an effective pressure that can, at least in principle, support the cloud against global collapse (Pudritz 1990).

Fatuzzo & Adams (1993) studied the mechanical forcing due to MHD waves propagat-

ing in a one-dimensional, self-gravitating slab. They considered two cases: a slab with an embedded magnetic field oriented parallel to the slab plane, and one with an internal field in the normal direction. In the first case, Fattuzzo & Adams showed that magnetosonic waves provide a normal force. In the second, it is Alfvén waves that exert the force, also in the normal direction. Thus, Fattuzzo & Adams verified explicitly that the waves counteract gravity, even in the absence of wave damping.

McKee & Zweibel (1995) extended this result. Using the pioneering analysis of Dewar (1970), they showed that Alfvén waves generated by a turbulent wave field exert an isotropic pressure, regardless of the background geometry. McKee & Zweibel derived a simple dependence of the wave pressure P on the local density:

$$P \propto \rho^{1/2} . \quad (1)$$

If we ignore the relatively small thermal pressure, then the cloud can be described as an $n = -2$ polytrope.

Are the structures of real clouds consistent with this polytropic wave pressure? One, indirect, argument indicates they are not. McKee & Zweibel also demonstrated that P is proportional to ρ times the square of the (randomly oriented) velocity fluctuation δv . It follows that

$$\delta v \propto \rho^{-1/4} \quad (2)$$

in this model. Now the density in an $n = -2$ polytrope tends to approach a power law outside the central plateau, such that ρ is proportional to $r^{-4/3}$. From equation (2), it follows that δv is proportional to $r^{1/3}$.

Consider the nearly spherical cloud, now gone, that produced the ONC. This cloud was recently driven off by the Trapezium stars, which themselves have ages of about 10^5 yr (Palla & Stahler 2001). The disruption itself occurred well within the cluster crossing time of about 10^6 yr. Hence, the present-day velocity dispersion of the *stars* should reflect the prior δv of the *gas*. But the dispersion of ONC proper motions has negligible variation from the center to the outskirts of the cluster (Jones & Walker 1988). These measurements span at least a decade in radius, over which δv should vary by a factor of 2.2, according to the polytropic relation.

Our conclusion, based on this admittedly limited evidence, is that a more realistic model of the internal turbulence has a spatially constant velocity dispersion.² If we further

²Inside giant cloud complexes, the observed velocity dispersion increases with the size of the substructure (Ossenkopf & Mac Low 2002). Again, we are focusing on a single clump, where such considerations do not apply.

appropriate the relationship between P and δv derived by McKee & Zweibel, we are then positing an isothermal equation of state:

$$P = \rho a_T^2 \quad (3)$$

Here a_T , the effective isothermal sound speed, is taken to be a fixed constant at a given instant of time. This same quantity varies temporally; indeed, this latter variation essentially drives the cloud’s evolution. We emphasize that a_T does not, as in ordinary gas dynamics, give the magnitude of random, microscopic velocities. Instead, this quantity represents, however crudely, the bulk motion of turbulent eddies; these eddies create the pressure P via MHD waves.

Since we are modeling the cloud as an isothermal sphere, we face the familiar difficulty that its mass is infinite unless the configuration is bounded externally. We therefore picture the cloud as being surrounded by a low-density, high-temperature medium with an associated pressure P_o . This latter quantity is also the pressure at the boundary of our spherical cloud. The cloud density at the boundary, ρ_o , is found from equation (3), given knowledge of a_T^2 .

2.2. Nondimensional Scheme

The mathematical description of a self-gravitating, isothermal cloud in hydrostatic balance is well known (see Stahler & Palla 2004, Chap. 9). All structural properties follow from the isothermal Lane-Emden equation:

$$\frac{1}{\xi^2} \frac{d}{d\xi} \left(\xi^2 \frac{d\psi}{d\xi} \right) = \exp(-\psi) , \quad (4)$$

with boundary conditions $\psi(0) = \psi'(0) = 0$. Here, ψ is the dimensionless form of the gravitational potential ϕ_g :

$$\psi \equiv \phi_g / a_T^2 . \quad (5)$$

The nondimensional radius ξ is obtained from the dimensional r using G , a_T^2 , and the central density ρ_c :

$$\xi \equiv \left(\frac{4 \pi G \rho_c}{a_T^2} \right)^{1/2} r . \quad (6)$$

Equation (4) was derived using both Poisson’s equation and the condition of hydrostatic equilibrium. The latter may be recast as a relation between the density at any radius, ρ , its central value, ρ_c , and the potential:

$$\rho = \rho_c \exp(-\psi) . \quad (7)$$

The full, dimensional mass M_o follows by integration of ρ over mass shells, Using equation (4) to evaluate the integral, one finds

$$M_o = \frac{a_T^3}{\sqrt{4\pi\rho_c G^3}} \left(\xi^2 \frac{d\psi}{d\xi} \right)_o . \quad (8)$$

Here, the subscript denotes the cloud boundary. Similarly, we shall use R_o for the radius of that point, where the internal cloud pressure has fallen to P_o .

In this standard formulation, all nondimensional variables are defined through the basic quantities a_T^2 , ρ_c , and G . Although the standard variables will remain useful, the scheme itself is not well suited to describing cloud evolution at fixed mass. For this purpose, we shall also utilize a second nondimensional scheme, based on M_o , P_o , and G .

Let λ be the new nondimensional radius, and α the nondimensional effective sound speed. These are defined through

$$\lambda \equiv \frac{P_o^{1/4}}{G^{1/4} M_o^{1/2}} r , \quad (9)$$

and

$$\alpha^2 \equiv \frac{a_T^2}{G^{3/4} M_o^{1/2} P_o^{1/4}} . \quad (10)$$

We further denote as δ the nondimensional density:

$$\delta \equiv \frac{G^{3/4} M_o^{1/2}}{P_o^{3/4}} \rho . \quad (11)$$

Since we will be discussing temporal evolution, we define a nondimensional time through

$$\tau \equiv \frac{G^{1/8} P_o^{3/8}}{M_o^{1/4}} t . \quad (12)$$

It will be useful to relate new nondimensional quantities to old ones. Thus, equation (6) tells us λ as a function of ξ :

$$\lambda = \sqrt{\frac{\alpha^2}{4\pi\delta_c}} \xi . \quad (13)$$

For the central density appearing here, δ_c , we use equation (7), evaluated at the cloud boundary:

$$\delta_c = \frac{\exp(\psi_o)}{\alpha^2} . \quad (14)$$

Finally, α itself may be written in terms of standard variables by using equation (8):

$$\alpha^4 = \sqrt{4\pi} \left(\xi^2 \frac{d\psi}{d\xi} \right)_o^{-1} \exp(\psi_o/2) . \quad (15)$$

3. Cloud Evolution

3.1. Internal Structure

We now consider a sequence of isothermal spheres of fixed mass, all embedded in the same external pressure. We may describe each structure using the new, nondimensional variables. The sequence is characterized by a single parameter, the center-to-edge density contrast; we shall denote this ratio as β . From equation (7), β can also be written as

$$\beta = \exp(\psi_{\circ}) \tag{16}$$

Since $\psi(\xi)$ is a known function, there is a one-to-one correspondence between our fundamental parameter β and ξ_{\circ} , the old, nondimensional radius. The potential ψ increases monotonically with ξ , so β likewise increases with ξ_{\circ} . The lowest value of β is unity, corresponding to $\xi_{\circ} = 0$.

The internal velocity dispersion α varies along our sequence. We may track this change through equation (15). Thus, for each selected β , we first find ψ_{\circ} from equation (16). From knowledge of the function $\psi(\xi)$, we find the corresponding ξ_{\circ} , as well as $(d\psi/d\xi)_{\circ}$. Equation (15) then yields α .

It is equally straightforward to obtain the internal density profile, $\delta(\lambda)$, of any model. Knowing ψ_{\circ} and α , equation (14) gives the central density, δ_c . Proceeding outward, equation (13) gives the value of ξ corresponding to each λ . Again using $\psi(\xi)$, equation (7) yields the density ratio, $\delta/\delta_c = \exp(\psi)$. When we get to the edge, $\lambda = \lambda_{\circ}$, we find that $\delta_{\circ}/\delta_c \equiv \beta^{-1} = \exp(-\psi_{\circ})$, in agreement with equation (16).

Figure 1 displays graphically the change of the cloud's structure as a function of β . Here we have plotted the radius, $\lambda(\beta)$, of selected mass shells. As expected, a shell in the deep interior monotonically shrinks. Other shells, however, turn around. With rising β , an increasing fraction of the cloud mass starts to expand. Such expansion costs energy. Thus, configurations of very high β are not physically accessible, as we shall see.

3.2. Enthalpy and Dynamical Stability

The lower dashed, horizontal line in Figure 1 corresponds to a β -value of 14.1. This is the Bonnor-Ebert density contrast. In the standard analysis, clouds of higher contrast are dynamically unstable (Ebert 1955; Bonnor 1956). We recall, however, that this instability arises from perturbations of a cloud *held at fixed temperature*. In contrast, our sequence has varying effective sound speed. The Bonner-Ebert contrast no longer marks a stability

transition. Nevertheless, this value, which we denote as β_{\min} , is still of interest. It signifies, at least in an approximate way, the point where self-gravity starts to overwhelm external pressure as the main compressive force. Our description of cloud evolution will henceforth focus on such gravity-dominated configurations, i.e., those for which $\beta > \beta_{\min}$.

To analyze stability in the present sequence, we first need to invoke thermodynamics. We showed in Paper I that energy dissipation in an isothermal cloud results in a decrease of the total enthalpy. Returning to dimensional notation, equation (A10) stated

$$\frac{dH}{dt} = -L , \quad (17)$$

where L is the luminosity. The enthalpy H is the generalization, to a self-gravitating gas, of the classic definition:

$$H \equiv E_{\text{therm}} + E_{\text{grav}} + P_{\circ} V , \quad (18)$$

where E_{therm} and E_{grav} are the thermal and gravitational potential energies, respectively, and V is the cloud volume.

To evaluate E_{therm} , we employ the general expression for a nonrelativistic gas, $(3/2) \int P dV$. Using equation (3) for P , this integral becomes $(3/2) M_{\circ} a_T^2$. Instead of evaluating E_{grav} directly, we invoke the virial theorem, in the form

$$E_{\text{grav}} = -2 E_{\text{therm}} + 3 P_{\circ} V . \quad (19)$$

After expressing the cloud volume in terms of the radius, the enthalpy is

$$H = -\frac{3}{2} M_{\circ} a_T^2 + \frac{16\pi}{3} P_{\circ} R_{\circ}^3 . \quad (20)$$

If we define a nondimensional enthalpy h through

$$h \equiv \frac{H}{G^{3/4} M_{\circ}^{3/2} P_{\circ}^{1/4}} , \quad (21)$$

then equation (20) becomes

$$h = -\frac{3}{2} \alpha^2 + \frac{16\pi}{3} \lambda_{\circ}^3 . \quad (22)$$

Figure 2 shows h along our sequence of clouds. Again, we restrict ourselves to gravity-dominated configurations, for which $\beta > \beta_{\min}$. We also recall that β increases monotonically along the sequence. Plotted here against α , the enthalpy dips to a minimum, then spirals inward toward a point. The latter corresponds to the singular isothermal sphere. For this special configuration, it may be shown that $\alpha^2 = (\pi/2)^{1/4}$ and $\lambda_{\circ} = (1/8\pi)^{1/4}$. Thus, the limiting value of h is -0.187 .

However, this limiting value is never reached in the course of evolution. As long as the cloud releases energy into space, so that $L > 0$, equation (17) tells us that the enthalpy declines. Thus, the last accessible configuration coincides with the minimum-enthalpy point in Figure 2. Numerically, we find that $h = -0.50$ for this cloud. The corresponding density contrast β is 370.

Consider now two configurations with identical values of h , very slightly above the minimum. These clouds, like all those in the sequence, have the same mass. We may view them as extremal states attained by the minimum-enthalpy cloud in the course of a normal mode of oscillation. Here, we are assuming that the cloud radiates negligible energy during an oscillation period, so that h remains constant. The two endstates are in precise force balance; intermediate states depart only slightly from this condition. In the small-amplitude limit, the oscillation has zero frequency, and the unperturbed, minimum-enthalpy, state represents a stability transition.

In summary, an isothermal cloud becomes dynamically unstable at a density contrast β of 370, provided the global enthalpy is held fixed during any oscillatory perturbation. This important fact was first discovered by Chavanis (2003) in the course of a general analysis of isothermal configurations.³ Note again the marked contrast with the traditional, Bonnor-Ebert result. The much lower critical density contrast in that case ($\beta = 14.1$) arises because the cloud releases – and draws in – as much energy as necessary to remain isothermal, even during a single oscillation period. This assumption would be inconsistent with our picture that the cloud is quasi-statically contracting due to relatively slow, turbulent dissipation.

The minimum-enthalpy state thus marks the natural endpoint of the cloud’s evolution. We denote as β_{\max} the corresponding density contrast, and display this limit as the upper dashed, horizontal line in Figure 1. Clouds with higher density contrast, including the singular isothermal sphere, are inaccessible.

3.3. Turbulent Dissipation

Although we have drawn a number of conclusions regarding the changing structure of our model cloud, we have yet to discuss its temporal evolution. The quasi-static contraction envisioned here is facilitated by the release of energy. This emission must arise at the shock interface between colliding, turbulent eddies. Typical fluid speeds are the virial value, i.e.,

³Chavanis finds a slightly higher critical β of 390. His minimum enthalpy value, in our units, is $h = -0.493$.

less than 10 km s^{-1} for the clouds of interest. Hence, the shocks radiate through far-infrared and submillimeter photons from low-lying transitions of molecules. The cloud is optically thin to such photons. The luminosity L in equation (17) is thus generated from the full interior.

Consider, then, a representative volume of the cloud. The numerical simulations mentioned previously have modeled the dynamics of a magnetized gas subject to an impressed, turbulent velocity field. Even if the fluid disturbances begin as incompressible Alfvén waves, efficient mode conversion produces compressible MHD waves that steepen and shock (see, e.g., Goldstein 1978). Significant energy is dissipated during the characteristic crossing time of the largest eddies. For example, Mac Low (1999) found that

$$\dot{\epsilon} = -\eta \frac{V_{\text{turb}}^3}{\lambda} . \quad (23)$$

Here $\dot{\epsilon}$ is the energy loss rate per unit mass of gas, V_{turb} the average (rms) eddy speed, and λ the dominate wavelength of the impressed turbulence. The empirical constant η was measured by Mac Low to be about 0.4.

In the simulations, turbulence is impressed on an arbitrary scale. Indeed, the question of what drives the turbulence remains controversial (Mac Low 2004). Here, we recall the key fact that the mean, interior velocities match the virial value over a large range of cloud sizes and masses (Larson 1981). It is likely, therefore, that self-gravity constitutes the basic driving mechanism, although a quantitative model is still lacking. If this basic idea is correct, then the “dominant wavelength” in equation (23) should be comparable to the cloud size. We therefore adopt, as our expression for the cloud luminosity L , a mass-integrated version of this relation:

$$L = \eta \frac{M_{\circ} a_T^3}{4 R_{\circ}} , \quad (24)$$

where the prefactor η does not necessarily have the value found by Mac Low. The factor of 4 in the denominator reflects the fact that the largest mode corresponds to overall expansion or contraction of the cloud (Matzner 2002).

3.4. Quasi-Static Contraction

To follow the cloud evolution in time, we use our prescribed luminosity to alter the global enthalpy. Combining equations (17), (20), and (24), we recast the result into nondimensional terms:

$$-\eta \frac{\alpha^3}{\lambda_{\circ}} = -6 \frac{d\alpha^2}{d\tau} + 64 \pi \lambda_{\circ}^2 \frac{d\lambda_{\circ}}{d\tau} . \quad (25)$$

The dependent variables α and λ_o are already known implicitly in terms of ξ_o . (Recall equations (13) – (15).) We may thus regard equation (25) as giving the dependence of τ on this same quantity. Since η is still unknown, we use instead the combination $\eta\tau$:

$$\frac{d(\eta\tau)}{d\xi_o} = \frac{6 \lambda_o}{\alpha^3} \frac{d\alpha^2}{d\xi_o} - \frac{64 \pi \lambda_o^3}{\alpha^3} \frac{d\lambda_o}{d\xi_o}. \quad (26)$$

We integrate this equation numerically, setting $\eta\tau = 0$ at $\xi_o = 6.5$, the value at the Bonnor-Ebert density contrast, and ending at $\xi_o = 25$, the minimum-enthalpy state. Over this evolutionary span, $\eta\tau$ increases by 0.96.

Figure 3 shows that neither the effective sound speed nor the cloud radius vary greatly during this period. The former increases monotonically, with a fractional change of 10 percent by the end. The radius gently decreases most of the time. Just before the unstable state is reached, the cloud surface begins to swell, in agreement with Figure 1.

The temporal change of the central density is much more dramatic. As seen in Figure 4, δ_c increases slowly at first, and then accelerates strongly at the end. Given the behavior of the cloud radius, this rapid compression evidently involves a small fraction of the total cloud volume. The left panel of Figure 5 displays the evolution of the full density profile. From bottom to top, the associated values of $\eta\tau$ are 0, 0.15, 0.23, and the final value, $\eta\tau = 0.24$.

Because the inner portion of the cloud undergoes such rapid compression, one may question the basic assumption of quasi-static behavior. Are all mass shells really moving at subsonic velocity? At the very center, the velocity must fall to zero at each time. But what of shells just outside the center?

Figure 6 shows the velocity profiles for the final three times depicted in the left panel of Figure 5. Since the temporal variable in equation (26) is $\eta\tau$, we plot the ratio $v/\eta\alpha$. For $\eta\tau = 0.60$ and 0.92 , the velocity is subsonic throughout, even if η were unity. In fact, plausible η -values are less than unity, as indicated earlier; we shall see in Section 4 below that $\eta \approx 0.3$ best matches the ONC data. In the final profile, corresponding to the minimum-enthalpy state, the peak velocities occur in the deep interior, and are mildly supersonic ($v \gtrsim \alpha$).

4. Modeling the ONC

4.1. Prescription for Star Formation

At present, we have scant knowledge of how the birthrate of stars scales with the properties of the cloud medium spawning these objects. Within the solar neighborhood, Schmidt

(1959) found the star formation rate to be proportional to the square of the local density; here, the rate is measure per unit volume. Schmidt’s law thus states that the formation rate per gas mass scales linearly with the cloud density.⁴

On the scale of galactic disks, it is established that the formation rate per unit disk area rises as Σ^n , where Σ is the total gas surface density, and the exponent n is about 1.4 (Kennicutt 1998). However, it is not straightforward to relate this important finding to the present study. Each areal patch in the galactic observations comprises numerous molecular complexes, any one of which is far larger than the clumps of direct interest here.

Returning to our model, if the clump indeed undergoes slow contraction, then its overall star formation rate must increase with time. It is plausible that the local rate within each mass shell rises with that shell’s density ρ . Following Schmidt, we posit a power-law dependence:

$$\dot{m}_* = \frac{\epsilon}{t_1} \left(\frac{\rho}{\rho_1} \right)^n . \quad (27)$$

Here, \dot{m}_* is the mass in stars forming per unit time, per unit cloud mass. The fiducial density and time, ρ_1 and t_1 , are those from equations (11) and (12), respectively:

$$\rho_1 \equiv \frac{P_\circ^{3/4}}{G^{3/4} M_\circ^{1/2}} \quad (28a)$$

$$t_1 \equiv \frac{M_\circ^{1/4}}{G^{1/8} P_\circ^{3/8}} . \quad (28b)$$

Finally, the exponent n is to be set by matching to observations. We stress that the prescription in equation (27) applies to low-mass stars. The formation of massive objects is a separate phenomenon. In our model, this occurs only in the high-density, central region of the final, minimum-enthalpy state.

Equation (27) contains a nondimensional efficiency factor ϵ . Since only a fraction of the cloud mass turns into stars, we expect ϵ to be well under unity. If, for simplicity, we assume this parameter to be the same in all mass shells, then integration of equation (27) yields the total mass per unit time in new stars:

$$\dot{M}_* = \frac{4 \pi \epsilon}{t_1 \rho_1^n} \int_0^{R_\circ} \rho^{n+1} r^2 dr . \quad (29)$$

⁴In Schmidt’s original formulation, the gas in question was HI. We now know, of course, that the relevant clouds are molecular.

We may conveniently recast this formula in terms of the effective sound speed:

$$\dot{M}_* = \epsilon \frac{a_T^3}{G} \mathcal{I} . \quad (30)$$

Here, the nondimensional quantity \mathcal{I} is expressed using the traditional, polytropic variables:

$$\mathcal{I} \equiv \frac{\alpha^{1-2n}}{\sqrt{4\pi}} e^{(n-1/2)\psi_0} \int_0^{\xi_0} e^{-(n+1)\psi} \xi^2 d\xi . \quad (31)$$

Our prescription gives a finite star formation rate for clouds of arbitrarily low density. This is clearly an oversimplification. There is no evidence, for example, that HI clouds form stars at all. Even within the molecular domain, it may be that stars form only above some threshold density. In their study of the Rosette cloud complex, Williams et al. (1995) found that only clumps which are strongly self-gravitating (as assessed by comparison of velocity dispersions, masses, and sizes) have internal stars. While a more complete model should account for this threshold effect, we shall not include it explicitly, but simply limit our discussion to self-gravitating clumps ($\beta > \beta_{\min}$) that are capable of forming stars.

4.2. Comparison with Observations

In Paper I, we empirically determined the star formation history of the ONC. The database of Hillenbrand (1997), together with theoretical pre-main-sequence tracks (Palla & Stahler 1999), allowed us to assign masses and contraction ages.⁵ In the detailed analysis, we restricted our attention to the 244 members with $M_* > 0.4 M_\odot$; the Trapezium stars themselves have $M_* \geq 7 M_\odot$, and are thus already on the main sequence. This sample is statistically complete, in the sense that the oldest stars do not fall below the observational sensitivity limit.

Based on our results from Paper I, Figure 7 shows $\dot{M}_*(t)$, the mass production per unit time, as a function of stellar age. Here, we have binned the data in age intervals of 10^6 yr. We have also extrapolated from our subsample to all stellar masses. We did so by multiplying the accumulated mass at each epoch by a factor of 1.3. This factor accounts for the missing stars with $M_* < 0.4 M_\odot$, according to the field-star initial mass function of Scalo (1998).

In order to use equation (30) to describe the ONC, we need the effective sound speed a_T as a function of time. Our numerical model gives the nondimensional functional relation

⁵Recently, Jeffries (2007) has redetermined the ONC distance as 390 pc, rather than the 470 pc used by Hillenbrand (1997). If correct, this distance shift will systematically lower stellar luminosities, and therefore increase their ages.

$\alpha(\eta\tau)$ (recall Fig. 3). Similarly, the quantity \mathcal{I} contains ψ_\circ and ξ_\circ , which we also know as functions of $\eta\tau$. Converting these relations to dimensional form requires that we set the cloud mass M_\circ and background pressure P_\circ .

We now make the critical assumption that the parent cloud of the ONC was, just prior to its dispersal, in the minimum-enthalpy state. Then equations (9) and (10) may be combined to yield

$$M_\circ = f_1 \frac{R_\circ a_T^2}{G} \quad (32)$$

and

$$P_\circ = f_2 \frac{G M_\circ^2}{R_\circ^4}, \quad (33)$$

where R_\circ and a_T refer to the final cloud state. The results of our numerical integration give $f_1 = 2.0$ and $f_2 = 0.028$. We take R_\circ to equal the radius of the stellar cluster (2.5 pc; see Hillenbrand 1997), and identify a_T with the observed *stellar* velocity dispersion (2.4 km s⁻¹; see Jones & Walker 1988). We then find that $M_\circ = 6900 M_\odot$ and $P_\circ = 1.1 \times 10^{-10}$ dyne cm⁻². The latter is about 300 times the canonical value in the diffuse interstellar medium, i.e., that bounding HI clouds (Wolfire et al. 1995).

It remains only to adjust ϵ , η , and the exponent n , until the theoretical star formation rate \dot{M}_* , as given by equation (30), matches the empirical one. We use a standard implementation of the Levenberg-Marquardt fitting algorithm (Press et al. 1988, § 15.5). The likelihood function that we maximize incorporates a uniform error in the star formation rate at each epoch of $\sigma = 3 M_\odot \text{ Myr}^{-1}$. Here we have used $\sigma \approx \sqrt{N} \langle M \rangle$, where N is the median number of stars produced per 10⁶ yr, and $\langle M \rangle$ is the average stellar mass at the appropriate epoch. This formula assumes that the number of stars in each bin is Poisson distributed about the mean predicted by the model, i.e., we neglect the observational contribution to the error.

The dashed curve in Figure 7 shows our theoretical rate as a function of stellar age, along with the optimal values for the three parameters. As predicted, ϵ is small (2×10^{-4}), signifying a low efficiency for stellar production. Specifically, the cloud converts 8 percent of its mass (550 M_\odot) into low-mass stars.⁶ The parameter η is also small (0.3), indicating that the cloud contracts over an interval long compared with the free-fall time, t_{ff} . The latter is 1.6 Myr for our initial cloud state. Finally, the best-fit value of n (1.4) lies close to unity. Thus, the original star formation law of Schmidt may hold quite generally. The 1-sigma

⁶This figure is higher if many of the embedded, near-infrared sources seen behind the ONC are members of the original cluster (Ali & Depoy 1995; Hillenbrand & Carpenter 2000).

errors in ϵ , η , and n , are, respectively, 1×10^{-4} , 0.08, and 0.09. These figures would have been larger had we included observational sources of error.

We note also that the basic physical characteristics of our model clouds are consistent with the clump properties inferred from observations. Our fiducial density ρ_o is equivalent to a molecular hydrogen number density of 520 cm^{-3} . As can be seen in Figure 5, the average interior density is higher by an order of magnitude. The mean visual extinction of a cloud, using $M_o/\pi R_o^2$ as the typical column density, is 11 mag. These figures are in general accord with the findings of Williams et al. (1995) for self-gravitating clumps in the Rosette complex. Moreover, A_v , measured inward from the edge, quickly exceeds unity in all our models. Thus, the hydrogen is indeed in molecular form throughout the bulk of the interior, as is appropriate for a star-forming cloud.

5. Discussion

In this paper we have adopted a conceptually simple model of cloud contraction and stellar group formation. The cloud is a self-gravitating sphere, supported against collapse by the motion of turbulent eddies. We assigned an effective pressure to this motion; our formulation implicitly assumes the eddy speed to be spatially constant, though varying in time. Cloud evolution is mediated by the slow leakage of energy, presumed to occur through internal, shock dissipation.

This model, supplemented by a Schmidt-type prescription for the star formation, can account not only for the empirically known history of the ONC, but also for more general characteristics of stellar birth. Consider, for example, the issue of formation efficiency. In the spirit of Krumholz & McKee (2005), we may define a nondimensional star formation rate per free-fall time:

$$\epsilon_{\text{ff}} \equiv \frac{t_{\text{ff}}}{t_{\text{ev}}} \frac{\Delta M_*}{M_o}. \quad (34)$$

Here, t_{ev} is the time over which the cloud produces stars, while ΔM_* is the total mass in these objects. Using our ONC model, and setting $t_{\text{ev}} = 1 \times 10^7 \text{ yr}$, we find $\epsilon_{\text{ff}} = 0.014$. Zuckerman & Evans (1974) long ago pointed out that only about 1 percent of the Galaxy’s molecular gas can become stars in a cloud free-fall time, to reproduce the observed, global star formation rate. The agreement here suggests that giant complexes create stars principally through their slowly contracting, internal clumps, as we have modeled.

We have not described, in any quantitative way, the physics underlying the turbulent dissipation. Our best-fit value of η for the ONC is similar to that found in numerical simulations of turbulent clouds (Mac Low 1999). However, our physical picture is quite

different. All simulations to date, which focus on an isolated, interior volume, find the turbulent energy dying away. In our model, the mean turbulent speed increases with time (see Figure 3). Future, global simulations of self-gravitating clouds supported by turbulent pressure should show this effect.

Our best-fit value of n agrees, perhaps fortuitously, with that originally proposed by Schmidt (1959). For an n -value of unity, the star formation rate per cloud mass scales with the gas density. Did this proportionality really hold in the ONC? The righthand panel of Figure 5 suggests that it did, at least roughly. Here, the solid curve is the density profile of our final, minimum-enthalpy, cloud model. The dot-dashed curve is the current number density of ONC stars, as reconstructed from the observed, projected number density (see Fig. 3 of Paper I). The similarity of the two curves indeed suggests that stars trace the mass distribution of the parent cloud. The same point is evident when comparing the projected stellar density with CO contours of the remnant gas (see Stahler & Palla 2004, Fig. 12.27).

Of course, all stars travel some distance from their birth sites. They do not move ballistically, but are subject to the gravitational potential of the parent cloud. Because of the star formation law expressed in equation (27), stellar births are indeed concentrated toward the cloud center, but there will inevitably be some outward diffusion. In a future paper, we hope to track this process through a direct, numerical simulation.

The minimum-enthalpy cloud that terminates our dynamical sequence is dynamically unstable. How do we interpret this instability in a more realistic setting? The essential fact is that the self-gravity of the gas becomes so strong that it leads to rapid, internal contraction, perhaps even true collapse of the central region. It is tempting to link this event with the formation of high-mass stars. While the physics of massive star formation is far from clear, the collapse or coalescence of dense, gaseous structures appears to play a key role (Stahler et al. 2000; McKee & Tan 2003). In the specific case of the ONC, the Trapezium stars are, of course, centrally located, and appear to be of relatively recent origin (Palla & Stahler 2001).

In comparing our model with data from the ONC, we have accepted at face value the stellar ages inferred from the placement of each object in the HR diagram. The age spread within clusters remains a contentious issue. For the ONC, Palla et al. (2005) have found that four nominally older stars are depleted in lithium, as would be expected. Such findings are inconsistent with the assertion by Hartmann (2001) that the ostensible age spread primarily reflects observational uncertainties.

Pflamm-Altenburg & Kroupa (2007) accept the higher ages, but hypothesize that all such stars were gravitationally captured from somewhat older, neighboring clusters. As the

authors themselves note, the existence of such neighboring systems is unclear. The other subassociations within the Orion complex are too young. One possibility is that there were a large number of nearby small groups producing low-mass stars and then dispersing. Pending more direct evidence for such groups, we continue to believe that the nominal age spreads in both the ONC and other systems are real.

In the present model, we have taken the cloud to be of fixed mass. This assumption may be acceptable for the ONC progenitor cloud, at least until the point when the Trapezium stars ionized and drove off the gas. In clouds producing low-mass T associations, the latter process does not occur. Yet these clouds are still dispersed, presumably through stellar winds. In our next paper, we will generalize our model of cloud contraction to include the effect of continuous mass loss. We will thus achieve a fuller picture of stellar group formation, a process of importance not only locally, but on galactic scales.

We are grateful to Steve Shore for pointing out the work of P. Chavanis on the thermodynamics of self-gravitating spheres. This project was supported by NSF grant AST-0639743.

REFERENCES

- Ali, B. & Depoy, D. L. 1995, *AJ*, 109, 709
- Arons, J. & Max, C. E. 1975, *ApJ*, 196, L77
- Bonnor, W. B. 1956, *MNRAS*, 116, 351
- Chavanis, P. H. 2003, *A&A*, 401, 15
- Dewar, R. L. 1970, *Phys.Fluids*, 13, 2710
- Ebert, R. 1955, *ZAp*, 37, 322
- Elmegreen, B. G. 2000, *ApJ*, 530, 277
- Elmegreen, B. G. & Scalo, J. 2004, *ARA&A*, 42, 211
- Falgarone, E. & Puget, J. L. 1986, *A&A*, 162, 235
- Falgarone, E., Puget, J.-L., & Pérault, M. 1992, *A&A*, 257, 730
- Fatuzzo, M. & Adams, F. C. 1993, *ApJ*, 412, 146
- Goldstein, M. L. 1978, *ApJ*, 219, 700

- Hartmann, L. 2001, *AJ*, 121, 1030
- Hartmann, L., Ballesteros-Paredes, J., & Bergin, E. A. 2001, *ApJ*, 562, 852
- Hillenbrand, L. A. 1997, *AJ*, 113, 1733
- Hillenbrand, L. A. & Carpenter, J. M. 2000, *ApJ*, 540, 236
- Huff, E. M. & Stahler, S. W. 2006, *ApJ*, 644, 355
- Jeffries, R. D. 2007, astro-ph/0701186
- Jones, B. F. & Walker, M. F. 1988, *AJ*, 95, 1755
- Kennicutt, R. C. 1998, *ApJ*, 498, 541
- Klessen, R. S., Burkert, A., & Bate, M. R. 1998, *ApJ*, 501, L205
- Krumholz, M. R. & McKee, C. F. 2005, *ApJ*, 630, 250
- Larson, R. B. 1981, *MNRAS*, 194, 809
- Mac Low, M.-M. 1999, *ApJ*, 524, 169
- Mac Low, M.-M. 2004, *Ap&SS*, 289, 323
- Mac Low, M.-M. & Klessen, R. S. 2004, *Rev. Mod. Phys.*, 76, 125
- Matzner, C. D. 2002, *ApJ*, 566, 302
- McKee, C. F. & Tan, J. C. 2003, *ApJ*, 585, 859
- McKee, C. F. & Zweibel, E. G. 1995, *ApJ*, 440, 686
- Ossenkopf, V. & Mac Low, M.-M., 2002, *A&A*, 390, 307
- Palla, F. & Stahler, S. W. 1999, *ApJ*, 525, 772
- Palla, F. & Stahler, S. W. 2000, *ApJ*, 540, 255
- Palla, F. & Stahler, S. W. 2001, *ApJ*, 553, 299
- Palla, F., Randich, S., Flaccomio, E., & Pallavicini, R. 2005, *ApJ*, 626, L49
- Pflamm-Altenburg, J. & Kroupa, P. 2007, *MNRAS*, 375, 855

- Press, W. H., Teukolsky, S. A., Vetterling, W. T., & Flannery, B. P. 1988, Numerical Recipes, Cambridge U. Press
- Pudritz, R. E. 1990, ApJ, 350, 195
- Scalo, J. 1998, in The Stellar Initial Mass Function, ed. G. Gilmore, I. Parry, & S. Ryan, Cambridge: Cambridge U. Press, 32
- Schmidt, M. 1959, ApJ, 129, 243
- Shirley, Y. L., Evans, N. J., Young, K. E., Knez, C., & Jaffe, D. T. 2003, ApJS, 149, 375
- Stahler, S. W. & Palla, F. 2004, The Formation of Stars, Wiley-VCH
- Stahler, S. W., Palla, F., & Ho, P. T. P. 2000, in Protostars and Planets IV, ed. V. Mannings, A. P. Boss, & S. S. Russell, Tucson: U. of Arizona Press, 327
- Tan, J. C., Krumholz, M. R., & McKee, C. F. 2006, ApJ, 641, L121
- Vázquez-Semadeni, E., Ballesteros-Paredes, J., & Klessen, R. S. 2003, ApJ, 585, L131
- Williams, J. P., Blitz, L., & Stark, A. A. 1995, ApJ, 451, 252
- Wolfire, M. G., Hollenbach, D., McKee, C. F., Tielens, A.G.G.M., & Bakes, E.L.O. 1995, ApJ, 443, 152
- Zuckerman, B. & Evans, N.J. 1974, ApJ, 192, L149

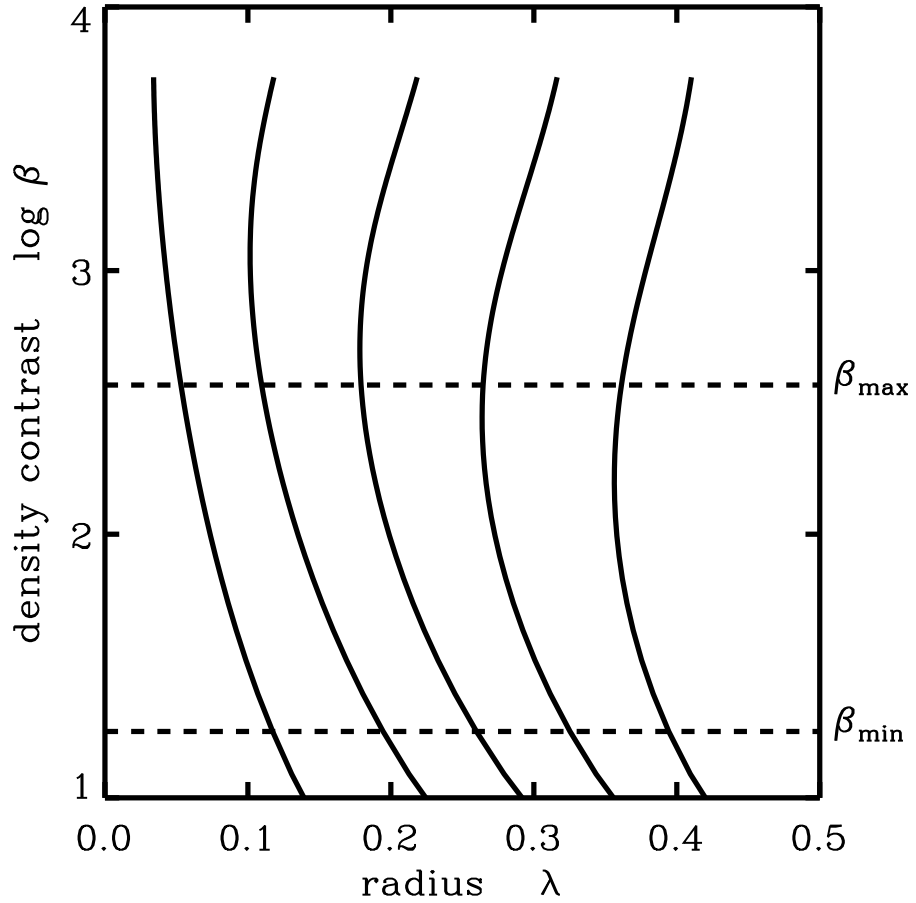


Fig. 1.— Evolution of the cloud’s internal structure. Shown are the radii of selected, Lagrangian mass shells as a function of the density contrast β . From left to right, the five shells enclose 0.2, 0.4, 0.6, 0.8, and 1.0 times the total cloud mass. Also indicated are the minimum β -value for self-gravitating clouds and the maximum value for dynamical stability.

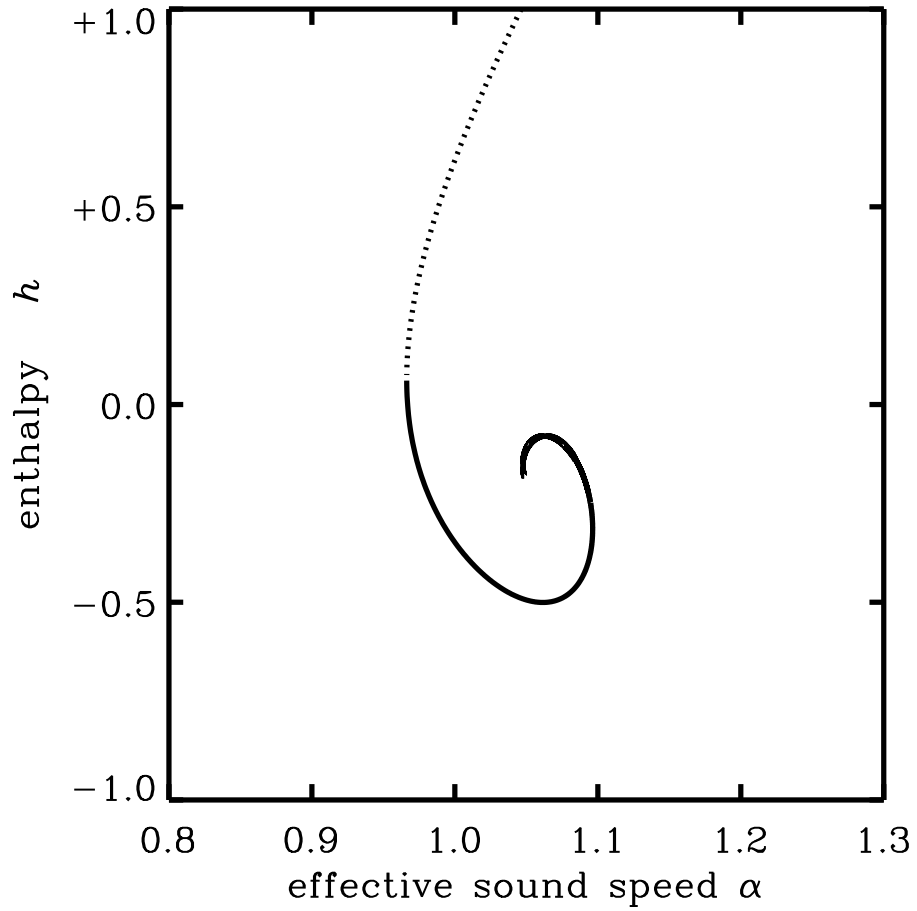


Fig. 2.— The run of specific enthalpy h along the cloud sequence. This quantity is plotted as a function of the effective sound speed α . The dotted portion of the curve pertains to clouds which have too low a density contrast to be self-gravitating.

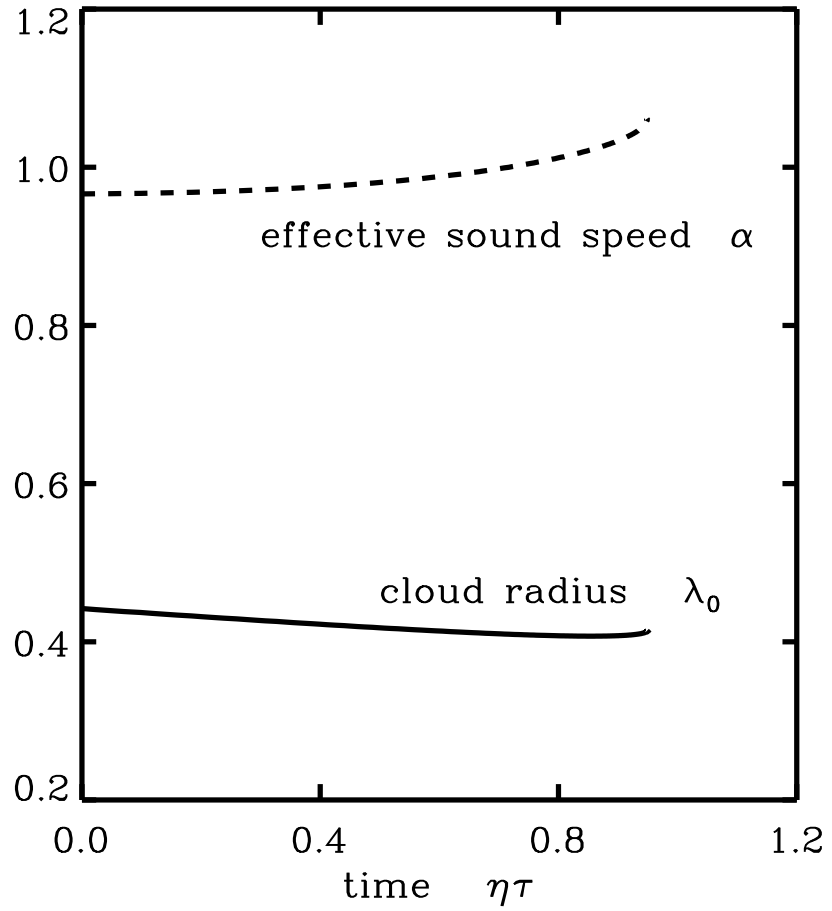


Fig. 3.— Evolution of the cloud radius (*solid curve*) and the effective sound speed (*dashed curve*). Notice that the time coordinate $\eta\tau$ starts at the first self-gravitating configuration, i.e., that for which $\beta = \beta_{\min}$.

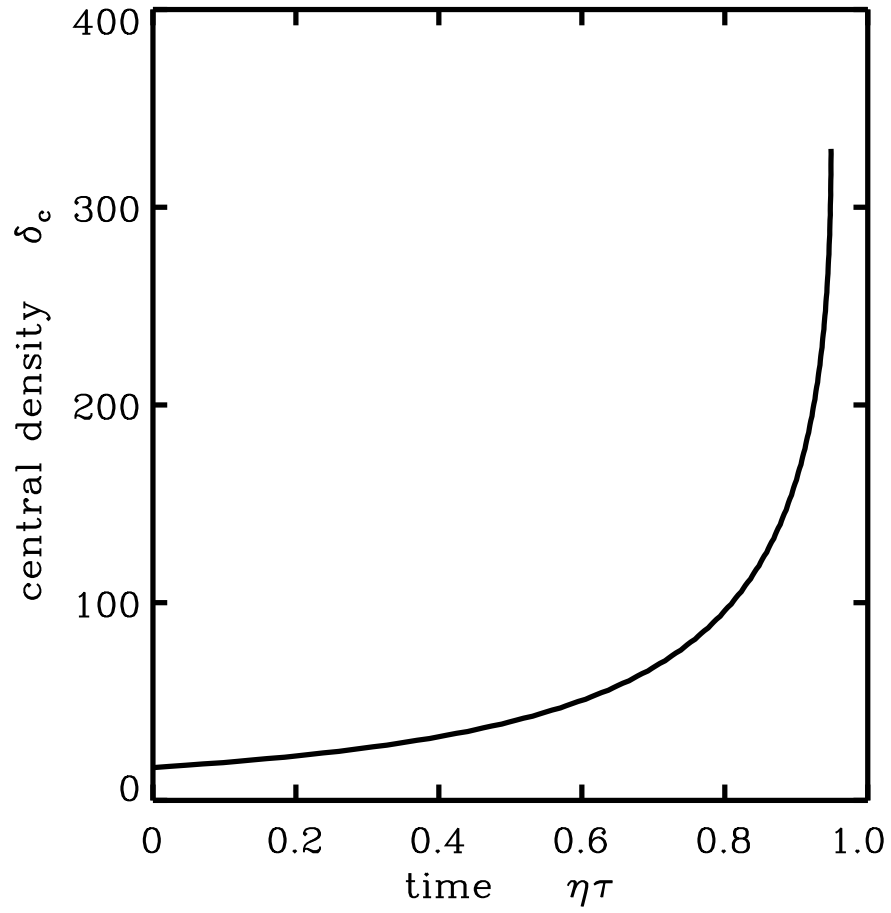


Fig. 4.— Evolution of the nondimensional central density. As in Figure 3, the time $\eta\tau$ is measured from the first self-gravitating cloud.

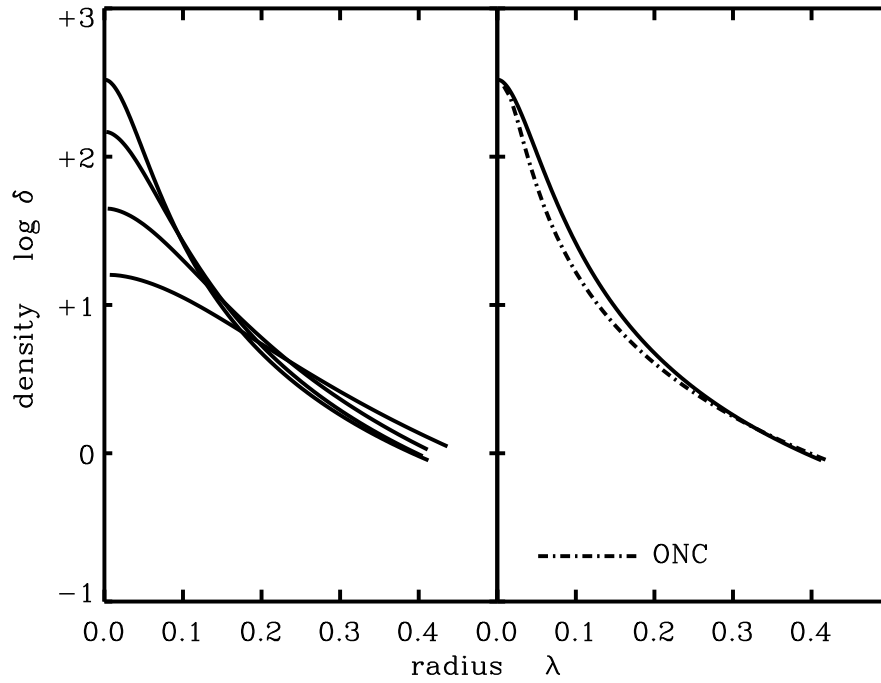


Fig. 5.— *Left panel:* Evolution of the density as a function of radius. From bottom to top, the corresponding values of $\eta\tau$ are 0, 0.60, 0.92, and 0.96. The latter value corresponds to the minimum-enthalpy state. *Right panel:* The density profile of the minimum-enthalpy state (*solid curve*) compared to the reconstructed stellar number density in the ONC (*dot-dashed curve*).

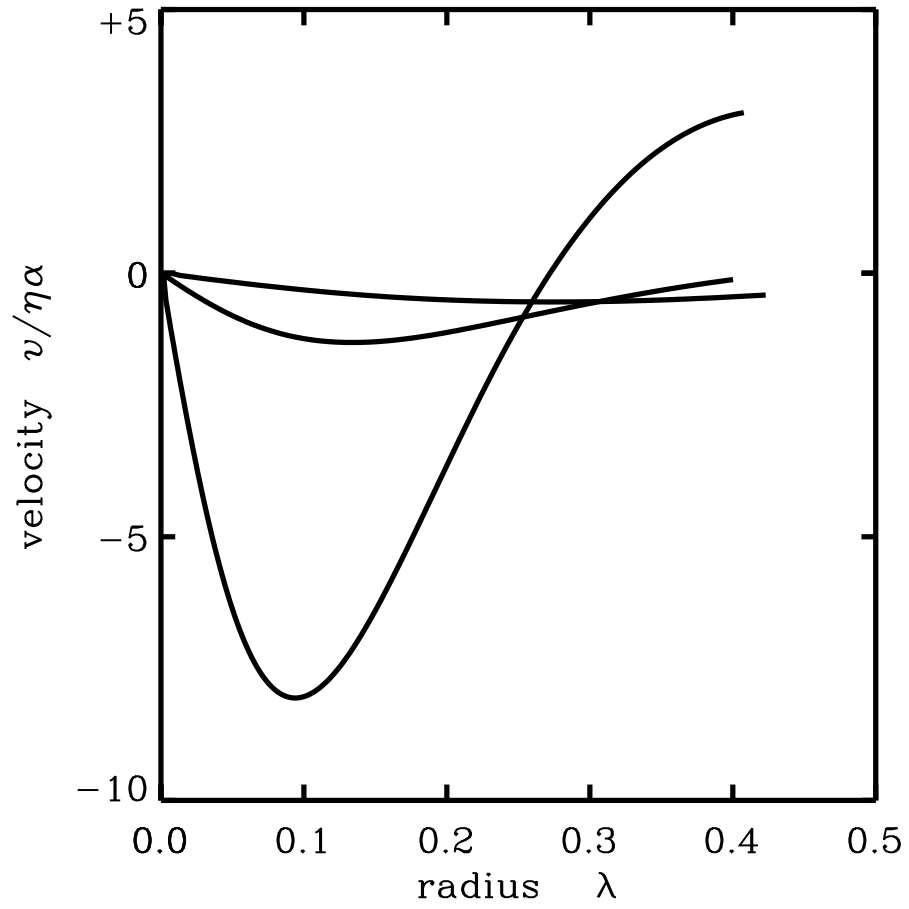


Fig. 6.— Evolution of the velocity profile. In order of deepening minima, the curves correspond to $\eta\tau$ -values of 0.60, 0.92, and 0.96. Note that the velocity is normalized to $\eta\alpha$.

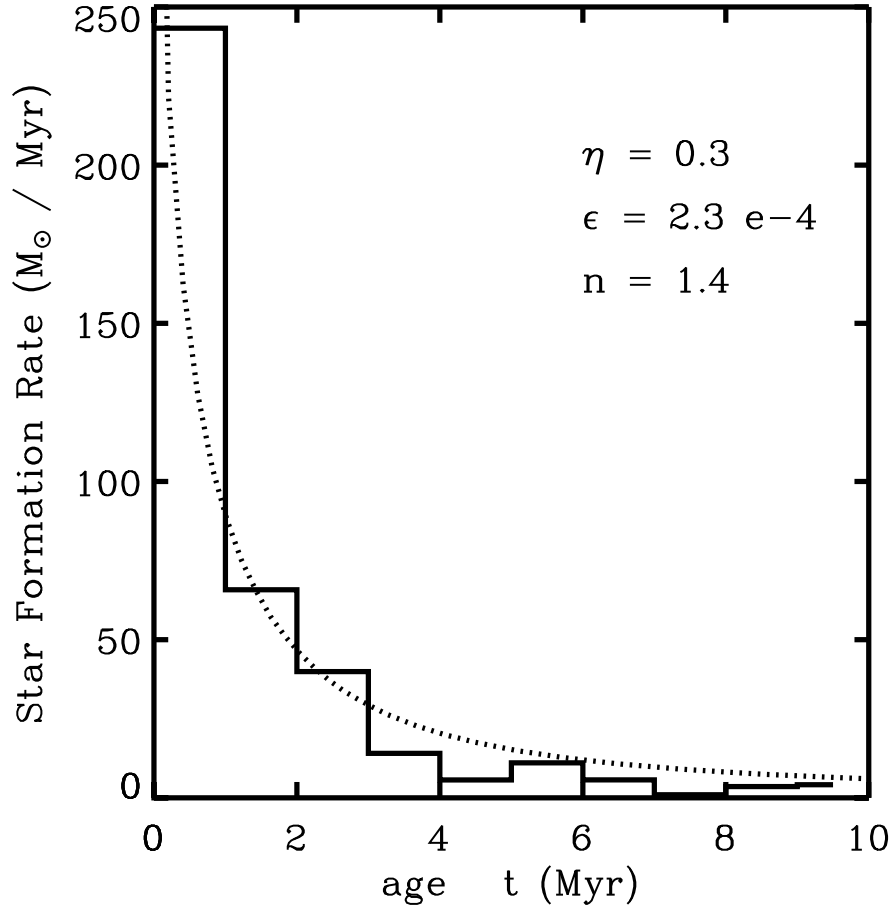


Fig. 7.— Total star formation rate in the ONC as a function of time. The latter is actually shown as the stellar age. The solid histogram uses the empirical ages from Paper I, binned in 1 Myr intervals. The dashed curve is the theoretical prediction. Also shown are the best-fit values for the model’s three free parameters: η , ϵ , and n .